

Electrochemical performance of decorated reduced graphene oxide by MoO₃ nanoparticles as a counter electrode

Mahyar Servati¹; Reza Rasuli^{1*}

¹Department of Physics, Faculty of Science, University of Zanjan,
P.O. Box 45371-38791

Abstract

We present an efficient electrocatalytic material based on anchored MoO₃ nanoparticles on reduced graphene oxide (RGO) nanosheets. After preparation of graphene oxide (GO), the MoO₃ nanoparticles anchored on GO nanosheet by using the arc-discharge method. X-ray diffraction patterns show that the MoO₃ nanoparticles are well crystallized on RGO in the orthorhombic crystalline phase with a crystallite size of 83 nm. In addition, FT-IR and Raman spectroscopy results show that during the arc-discharge process, the GO nanosheets have been reduced and RGO nanosheets are decorated with MoO₃ nanoparticles which form a porous structure. The surface energy of the prepared electrode was measured as 44.56 mJ/m², which shows the desirable spreading ability of the electrolyte on the electrode. Finally, electrochemical performance was measured in the symmetrical dummy cell by impedance spectroscopy and cyclic voltammogram, and the photochemical test was measured in the dye-sensitized solar cell by current density measurement. Our results show that the electrochemical performance of the RGM electrode is better than the RGO electrode and is comparable with the Platinum electrode and also the efficiency of RGM electrode used in a dye-sensitized solar cell as a counter electrode is 5.55% near to Platinum electrode performance.

Keywords: MoO₃ nanoparticles, Graphene oxide, electrocatalytic, solar cell

* Corresponding author: Tel.: Fax: +98 241 2283203. E-mail address: r_rasuli@znu.ac.ir (Reza Rasuli)

1. Introduction

Enhancing the performance of electrochemical and electrocatalytic is important for energy storage and conversion in various devices such as batteries, capacitors, fuel cells, and solar cells [1-3]. In recent years, organic solar cells which are based on electrochemical reactions have attracted remarkable attention of researchers due to the facile and inexpensive production process and an average efficiency of about 12–14% [4-6]. The main effort of the researchers is to reduce production costs, increase efficiency and raise the stability of these type of solar cells [7, 8].

Using organic compounds instead of current costly materials is a challenge towards achieving these three aims [9-12]. In a solar cell, the counter electrode is one of the deterministic components which affects the performance of the cell. For instance, in a dye-sensitized solar cell, by light radiation on the dye molecules, electrons excite and flow into the circuit and then collect via a counter electrode from the external circuit and inject into the electrolyte to reduce dye molecules again [8, 13-15]. In such a system, the counter electrode plays a crucial role to complete this cycle in order to produce a photocurrent. To improve this electrode, researchers have conducted a wide range of their studies on carbonaceous materials for energy conversion and storage, due to its low-cost availability, high chemical stability, proper electrical conductivity as an alternative for platinum [16].

Among carbonaceous materials, graphene has drawn extensive attention as a promising material because of high surface area ($2630 \text{ m}^2 \text{ s}^{-1}$) and fast charged carrier mobility ($200,000 \text{ cm}^2 \text{ V}^{-1} \text{ s}^{-1}$) [17-20]. In electrochemical devices, the number of active sites determines the rate of electrochemical reactions and this site typically located in defects and crystal edges [21]. Enhancing defects and functional groups in graphene allows us to increase the active sites for improving electrocatalytic activity. These factors can be controlled by heating the graphene oxide (GO), and results show that by proper heat treatment of GO, the electron transfer resistance can be reduced to less than 1.20 ohm.cm^2 [22]. On the other hand, reducing graphene oxide (RGO) causes eliminate the functional groups in graphene sheets and their active sites in porous structure [23]. Counter electrode can be improved by embedded catalytic nanoparticles between graphene sheets which maintain the electrical conductivity while improving the porous catalytic sites [24].

The MoO_3 nanoparticle as an n-type semiconductor with [25] multiple valence states and high chemical and thermal stability, is an efficient material for this purpose, which previously used in organic LED, Li-ion batteries applications and electrocatalyst for Hydrogen Evolution Reaction [26-31]. There is no report on reduced graphene oxide nanosheets functionalized with MoO_3 nanoparticles (RGM) as an electrochemical catalyst for I^-/I_3^- redox couple reaction in dye-sensitized solar cells. Triiodide/iodide redox is a common

electrolyte in dye-sensitized solar cells and lithium-iodine batteries [12, 32]. Nanostructured MoO₃ in proximity to graphene can be used as a counter electrode for application in organic photovoltaic cells. At the interface of graphene and MoO₃ nanoparticles, high work function and ionization energy of MoO₃ nanoparticles cause to flow down the electrons to MoO₃ nanoparticles in order to maintain the thermodynamic equilibrium. This creates a large dipole and increases the hole concentration in the interface of graphene and MoO₃ nanoparticles and led to the band bending in MoO₃ below to the Fermi level of graphene. As a result, the electron transfer barrier is almost zero and this junction treats similar to a usual metal, and n-type semiconductor junction [33-36]. However, its reaction as an electrocatalyst material with triiodide/iodide redox is not studied yet.

In the following, we will introduce a facile method for synthesis and characterization of RGO nanosheets doped with MoO₃ nanoparticles. Then electrochemical test in symmetrical dummy cell will be shown, and the efficiency of the Platinum cathode (Pt) as a reference and RGM electrode obtained by Arc discharge method comparing with RGO electrode which obtained from reduced GO by hydrazine hydrate will be shown in the dye-sensitized solar cell. Electrolyte diffusion in the prepared electrode was explored by the surface energy measurement and finally, the performance of the solar cell made with the prepared counter electrode was investigated by the J-V curve measurement.

2. Experimental

Graphene Oxide synthesis

The graphene oxide used in this work, synthesized by improved Hummers and Offeman method [37] that have been reported previously [38]. In brief, 15 ml Sulfuric acid added to 1.0 g graphite powder from Sigma Aldrich (45 μ m powder) and stirred at 27 °C for 15 min. Then In the ice bath, the 3.0 g of potassium permanganate added slowly to the solution. The mixture stirred for 2 h at 40 °C with speed of 1200 RPM. Afterward 300 ml deionized water added to the solution. Using DI water and centrifuge successively, the remaining acid was removed from the solution. To exfoliate graphite oxide to graphene oxide, the solution was exposed in ultrasound waves for 1.5 h and finally was centrifuged to achieve a homogenous dark brown solution.

RGM synthesis

To decorate MoO₃ nanoparticles on GO nanosheets, we used the arc-discharge method by semi-auto arc discharge device [38, 39]. Two molybdenum electrodes as the cathode and anode with 3 mm diameter and

99.8% purity were placed in GO aqueous solution. Then 10 A currents applied between these two electrodes for 15 minutes. A micrometer screw setting was used to adjust the separation distance between the electrodes. As a result, MoO₃ nanoparticles were ablated from the anode and then condensed on the GO solution. The heat generated by the arc-discharge reduced the GO functional groups and stabilized the MoO₃ nanoparticles simultaneously and RGM suspension was obtained.

Symmetrical dummy cell preparation

To investigate the electrochemical activity symmetrical dummy cell was fabricated from two clean Fluorine-doped Tin Oxide glass (FTO) coated by drop casting method of RGM suspension at 75 °C temperatures. Then they were annealed at a temperature of 400 °C for 2 hours to reduce GO nanosheets completely, crystallizing MoO₃ nanoparticles and stabilize material on the FTO glass. These identical cathodes with an active area of 0.1962 cm² assembled face to face with a 60 μm thick tape as a spacer and sealing. Then the electrolyte (10 ml ethylene glycol, 830 mg potassium iodide, and 127 mg iodine crystals) was injected to cell through a hole on one FTO glass and then closed by a sealing tape.

Photoelectrochemical cell preparation

To study on prepared cathode's performance in Dye-sensitized solar cell, Photoelectrochemical cell was fabricated. The TiO₂ photoanodes were made of TiO₂ paste (9 gr TiO₂ powder, 1.5 mL acetic acid, 0.2 mL surfactant) with the Doctor Blade method on clean FTO glass and then annealed at 325 °C, 375 °C, 450 °C, 500 °C for 5, 5, 15, 15 min respectively to crystallize TiO₂ nanoparticles. To sensitize TiO₂ nanoparticles, photoanodes were soaked overnight in N719 solution (0.3 mM in a mixed solvent of acetonitrile and tart-butanol with a volume ratio of 1:1). The solar cell was assembled with a dye-sensitized photoanode and RGM, RGO and Pt cathodes, with an active area of 0.1962 cm². The cathodes were separated by 60 μm thick tape as a spacer and sealing. The electrolyte was injected to cell through the hole on FTO glass, then closed by the tape.

Characterization

Fourier transform infrared (FT-IR) spectra were measured with a Thermo Scientific Nicolet iS10 FT-IR spectrometer. The X-ray Diffraction (XRD) experiments were performed using a Philips X-ray diffractometer model PW 1730 by a Cu *k*_α radiation source with a wavelength of 1.54 Å. Scanning electron microscopy (SEM) and Field Emission Scanning Electron Microscopy (FESEM) were carried out using a TESCAN VEGA-II and TESCAN MIRA-III, respectively. Raman spectroscopy was recorded by Rigaku Handheld Raman Analyzer model FirstGuard with an excitation wavelength of 1064 nm. Electrochemical measurements were performed by using the OGFOIA and OGFEIS multi-channel system of Electrochem

Originals Company of symmetrical dummy cells. Impedance spectra were measured at 0 V bias voltage and the modulation amplitude of 10 mV, in the frequency range from 65 kHz to 100 mHz. The data of impedance spectra were fitted using Zplot/Zview software. The CV curves were measured at a scan rate of 10 mV/s in 600 to -600 mV voltage range. J-V curves were measured at AM 1.5 G with a radiation power of 100 mW/cm² by IV100 Cyclic Voltammetry from Safir Soraya Sepahan Company.

3. Results and discussion

Using Fourier transform spectroscopy, we studied the reduction process of GO. Figure 1 shows the comparison between the synthesized GO, reduced GO nanosheets by hydrazine hydrate, and RGM obtained by arc discharge method. By adding hydrazine hydrate to the GO, as shown in Figure 1, the functional groups are well reduced. The peak at 3415 cm⁻¹ is the characteristic of the O–H bonds due to adsorbed water molecules. The C-H vibrations appear at 2922 cm⁻¹ and the peaks at 1730 and 1398 cm⁻¹ are correspond to C=O and C-O bonds, respectively. As shown in Figure 1 these peaks have completely disappeared in the RGO and RGM. The peak at 1622 cm⁻¹ corresponds to the carbonic bond in graphene, which is observed for all spectra. The C-O-C bond appears at 1077 cm⁻¹ and its intensity slightly decreases in both reduction methods [40, 41]. The 1000–400 cm⁻¹ peak in RGM corresponds to the vibrations of metal-oxygen characteristic bonds. The peak at 615 cm⁻¹ is oxygen bonding with three molybdenum atoms. The peaks at 991 and 877cm⁻¹ are due to the formation of Mo⁶⁺ atoms bonding with oxygen in the Mo=O and Mo-O-Mo forms, respectively showing crystallization in the orthorhombic phase [25].

To investigate surface morphology, the FESEM images were taken from the prepared GO and RGM powder. As seen in Figure 2, GO plates are well exfoliated and we can see MoO₃ nanoparticles with the average size of about 20 nm were anchored uniformly on RGO curved nanosheets.

In Figure 3, the X-ray diffraction spectra of the annealed MoO₃ and RGM samples have been presented. In MoO₃, the highest intensity of the X-ray diffraction spectrum is due to the (021) plane, which indicates the crystallization of MoO₃ in the orthorhombic crystalline phase (α -MoO₃) with the spatial group of Pbnm (a = 3.96 Å, b = 13.85 Å, c = 3.69 Å). To calculate the crystallite size, we used the Scherrer's equation as follow:

$$\tau = \frac{K\lambda}{\beta \cos(\theta)}, \quad (1)$$

Where K is the shape factor (= 0.9), λ is the X-ray wavelength (= 0.154nm), β is the line broadening at the half maximum intensity and θ is the Bragg angle. According to XRD results, the crystallite size of the MoO₃ obtained about 83 nm. In the RGM spectrum, in addition to the MoO₃ peaks, three sharp diffraction peaks are

seen at 12.94°, 25.85° and 39.15°, which related to the GO and RGO nanosheets [42-44]. By using Bragg's diffraction law, the spacing of the nanosheets was estimated and the distance between nanosheets for a peak at 12.94° and 25.85° is 6.83, and 3.44 Å, respectively. The high intensity of the RGO peak indicates a significant reduction of GO. The peak at 39.1° with a spacing of nanosheets is equal to 2.3 Å is probably due to a short range order and incomplete oxidation cause them to accumulate [42]. The average crystallite size of the RGM by Scherrer's equation is calculated about 331 nm which shows anchoring of the MoO₃ nanoparticles on the RGO.

Raman spectroscopy was used to investigate the structure of the prepared samples (Figure 4). In a typical Raman spectrum of GO, the D peak at 1290 cm⁻¹ is breathing mode which is related to the defects and disorders of GO and the G peak at 1599 cm⁻¹ represents the graphitized structure and coplanar vibration of sp²-bonded carbon atoms in the two-dimensional hexagonal lattice [45]. In comparison with GO, the intensity of D band relative to G band in the RGM spectrum increases to 1.22, which shows more defects in the structure and high porosity of RGM [46, 47]. According to the empirical equation $L_a \text{ (nm)} = (2.4 \times 10^{-10}) \lambda^4 (I_G/I_D)$, the crystallite size of the graphitic carbon is about 252 nm that λ is laser excitation wavelength (1064 nm) [48]. In addition, by comparing the G peak for GO and RGM, the peak has a blue shift indicating the strong bond of nanoparticles to the RGO nanosheets. The peaks at 816 and 976 cm⁻¹ are related to the symmetrical and asymmetrical Mo=O stretching vibrations. The peaks at 656 cm⁻¹ are assigned to the stretching vibration of O-Mo-O bonds and peaks below 600 cm⁻¹ are related to the bending vibrations of the α -MoO₃ crystal [46, 49, 50].

Morphologies, surface porosity and cross thickness of the RGM electrode were examined by scanning electron microscopy. Figure 5 (a) shows the SEM images from the anchored MoO₃ nanoparticles on the RGO sheets. As shown in Figure 5 (b), after annealing at 400 °C, the nanoparticles are crystallized in a larger size with proper porosity and formed in a columnar shape. Figure 5 (c) exhibit the cross-section of the electrode which shows a layer with a thickness of about 4.5 μm .

In this part, we study the diffusion rate of electrolyte in the RGM electrode. For this purpose, the surface energy by Neumann method was measured. Using the contact angle of five deferent fluids on the electrode surface (as presented in Table 1) and Neumann's equation of state we obtained the surface energy according to the Eq. 2 [51]:

$$\cos(\theta) = -1 + 2 \sqrt{\frac{\gamma_s}{\gamma_L}} e^{-\beta(\gamma_s - \gamma_L)^2} \quad (2)$$

In Eq. 2, θ is the contact angle of the applied liquid, γ_s is the surface energy of the substrate, γ_L is the surface energy of the liquid and β is a constant. According to the fitted curve in Figure 6 and data in Table 1, the surface energy of RGM was calculated as 44.56 mJ/m². These results indicate that the RGM electrode is suitable for diffusion of organic electrolytes which can rapidly spread over the electrode surface where ions can react with the electrons.

To characterize the electrochemical activity, the electrochemical impedance measurements and cyclic voltammogram were carried out in a symmetrical dummy cell. By this experiment, the electrochemical performances parameter such as charge transfer resistance at the cathode, electrolyte interface (R_{CT}), and overall cell resistance (R_S), can be obtained. In Figure 7 the Nyquist plot of electrodes fabricated with Pt, RGO, and RGM are presented. The left inset in this figure shows the magnified curve in the high-frequency region and the right inset indicates an equivalent circuit for fitting Nyquist plot. In this circuit, R_S is the overall Ohmic serial cell resistance. R_{CT} is the charge transfer resistance and CPE is the constant phase element arises from the roughness of the electrodes where describes the deviation from ideal capacitance. Z_w is Nernst diffusion impedance of the triiodide/iodide redox couple in the electrolyte and $Z_{w,pore}$ (that introduced by Mayhew *et al.* [9]) for porous carbon electrodes, is the Nernst diffusion impedance in the porous materials where occurs at high-frequencies.

As we can see in the left inset of Figure 7, Pt acts as a catalytic non-porous surface and the $Z_{w,pore}$ parameter did not appear. So that the high-frequency intercept on the real axis is attributed to the serial resistance (R_S) and the first semicircle in the high-frequency region is evaluated as the R_{CT} and the corresponding CPE at the electrode and electrolyte interface. The second semicircle in the low-frequency range arises from Nernst diffusion of electrolyte species (Z_w).

The Nyquist plot of RGO and RGM in Figure 7, due to their porous structure, exhibit the high-frequency semicircle that resulting from diffusion through the electrode pores ($Z_{w,pore}$). The slight increase in the $Z_{w,pore}$ of RGM compared with RGO is probably due to the increase in porosity, thus resists against the electrolyte species diffusion in porous structures. In the higher frequency region, the offset value of the real axes indicates the R_S of each sample. In the middle-frequency region, second large semicircle in the RGO and RGM Nyquist plot is determined as R_{CT} and corresponding CPE at the interface of electrode and electrolyte. The R_{CT} of RGM is extremely decrease compared to RGO. This is due to an increase in the surface area of RGM compared to RGO, therefore enhance the electrocatalyst activity. These results are summarized in Table 2. The third semicircle in the low-frequency region due to diffusion impedance of the triiodide/iodide redox couple in the electrolyte is not observed probably because of overlapping with the second semicircle.

We also carried out the cyclic voltammogram test from symmetrical dummy cells with Pt, RGM, and RGO counter electrode. The voltage range was applied between -600 and 600 mV with a scan rate of 10 mV/s. As shown in Figure 8, the maximum current is related to the Pt, RGM, and RGO, respectively. Also, by calculating the slope inverse of the voltammogram curve at zero voltage, it can be approximated to the overall cell resistance [52, 53]. The values for Pt, RGM, and RGO are equal to 0.25, 0.36 and 0.41 Ω respectively. To characterize the performance of the RGM electrode in an applicable device, we used it in a dye-sensitized solar cell and measured the J-V curve as presented in Figure 9. The photovoltaic parameters indicated in Table 2. The open circuit voltage (V_{OC}) is the maximum voltage generated by a solar cell. As shown in the schematic of energy levels in Figure 10, in a dye-sensitized solar cells, V_{OC} is the voltage difference between the oxidation in photoanode and reduction in RGM electrode of the dye molecules. The short-circuit current (I_{SC}) is the current through the solar cell when the voltage across the solar cell is zero. By decreasing the overall series resistance of the cell, the I_{SC} increases. Fill Factor (FF) is an interpreter of a deviation from an ideal solar cell that defined as the ratio of the maximum power from the solar cell to the product of V_{OC} and I_{SC} . A solar cell with less R_{CT} and R_s shows better FF which is attributed to the increased electrocatalytic performance of cathode materials.

To compare the performance of RGM electrode we used the Platinum electrode as a reference and RGO cathode as a base carbon material, with the same photoanode. According to Table 2, the open-circuit voltage (V_{OC}) of the RGM electrode enhances compared with platinum and RGO electrodes. Increasing the porosity in the RGM electrode provides a sufficient number of catalytic sites for electrolyte ions to reduce. R_s reduction leads to increasing I_{SC} of Pt and RGM electrodes in comparison with RGO. As we expected, FF enhanced due to the decrease of R_{CT} in RGM electrode compare with RGO and these results lead to the close efficiency of the RGM electrode to the platinum electrode.

Conclusions

In this study, we introduced decorated RGO with MoO_3 nanoparticles as a cost-effective counter electrode with good chemical stability and catalytic performance for I_3^- reduction. We presented a facile method to anchor the MoO_3 nanoparticles on the GO nanosheets using the arc-discharge method (Figure 11) and our results exhibit that anchored MoO_3 nanoparticles are well crystallized on RGO. In addition, FTIR and Raman spectra confirm that the GO reduces and the MoO_3 nanoparticles anchored as well on RGO during the arc-discharge process. The low surface energy of the counter electrode shows easy spreading and diffusion of electrolytes in it. Finally, the characterization of electrochemical activity by impedance measurements and

cyclic voltammogram results showed that incorporation of MoO₃ nanoparticles with RGO nanosheets improve porous structure without degradation electrical conductivity of RGO, so that have a significant impact on the electrochemical efficiency. According to some previous reports of organic materials used in the counter electrode in dye-sensitized solar cell which shows in Table 3, the performance of the dye-sensitized solar cell assembled by RGM electrode indicates that this low-cost electrode can be an appropriate alternative to the Pt electrode in electrochemical cells with acceptable efficiency.

Acknowledgment

This work has been supported by Iran National Science Federation (ISNF) under Grant No. 94809262. The authors also thank Dr. Hasan Shayani-Jam, Pouria Moradi for their kind assistance.

Table 1: The surface tension and the contact angle of five different fluids.

liquid	γ_L (mJ/m ²)	CA (degree)
Water	72.8	95
Ethylene Glycol	47.99	64.2
1-Methyl-2-Pyrrolidinone	40.79	20
n-Hexane	18.4	0
Acetone	25.2	0

Table 2: Photovoltaic parameters of RGM and Pt counter electrodes

Parameters	I _{sc} (mA)	V _{oc} (mV)	FF (%)	Efficiency (%)	R _s (Ωcm^2)	R _{CT} (Ωcm^2)
RGO	2.16	708	55.4	4.32	8.41	124.43
RGM	2.3	752	63	5.55	5.88	32.48
Pt	2.27	696	72.4	5.83	5.22	6.11

Table 3: Electrocatalytic properties of various carbon Counter Electrodes in Dye sensitized solar cells

Counter Electrode	J _{sc} (mA/cm ²)	V _{oc} (mV)	FF (%)	Efficiency (%)
functionalized graphene sheets [9]	7.77	710	70	3.83
Graphene Nanosheets [54]	13.42	690	71	6.45
Nitrogen-doped porous carbon [55]	15.58	702	63	7.01
MoS ₂ /Graphene [56]	17.24	714	63.83	7.86
Mesoporous carbon [57]	14.32	733	58	6.06
Sub-micrometer-sized Graphite [58]	12.7	794	62	6.2
Nickel selenide/reduced graphene oxide [59]	19.94	751	65	9.75
Current work (RGM)	11.72	752	63	5.55

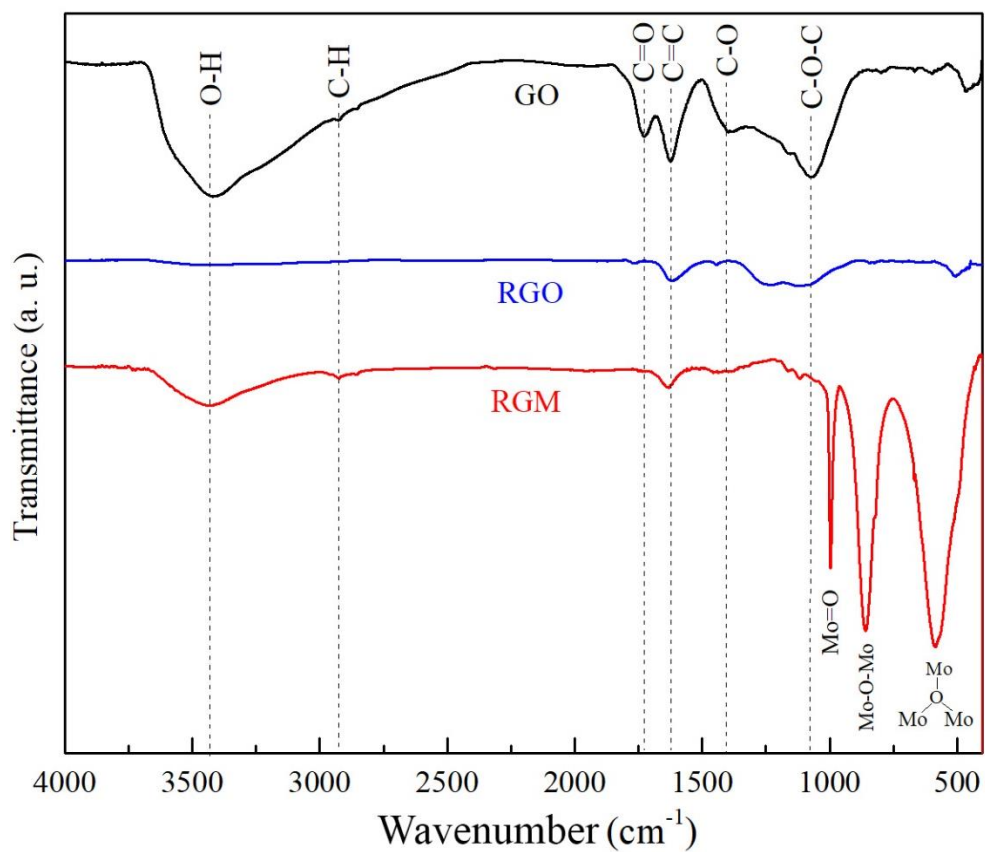


Figure 1: FTIR analysis of GO and RGO Compare to RGM

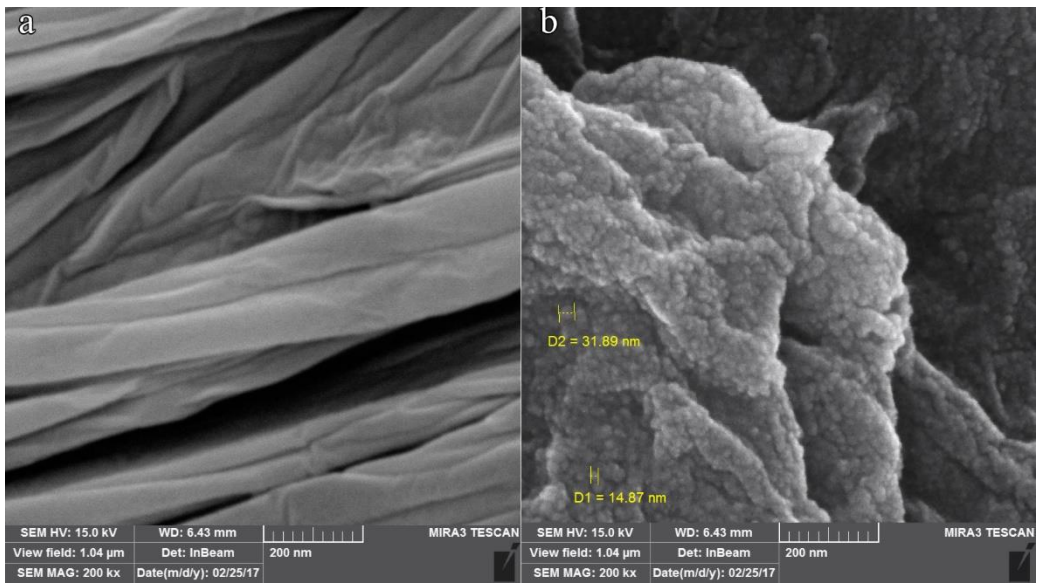


Figure 2: FESEM images of (a) GO nanosheets and (b) RGM.

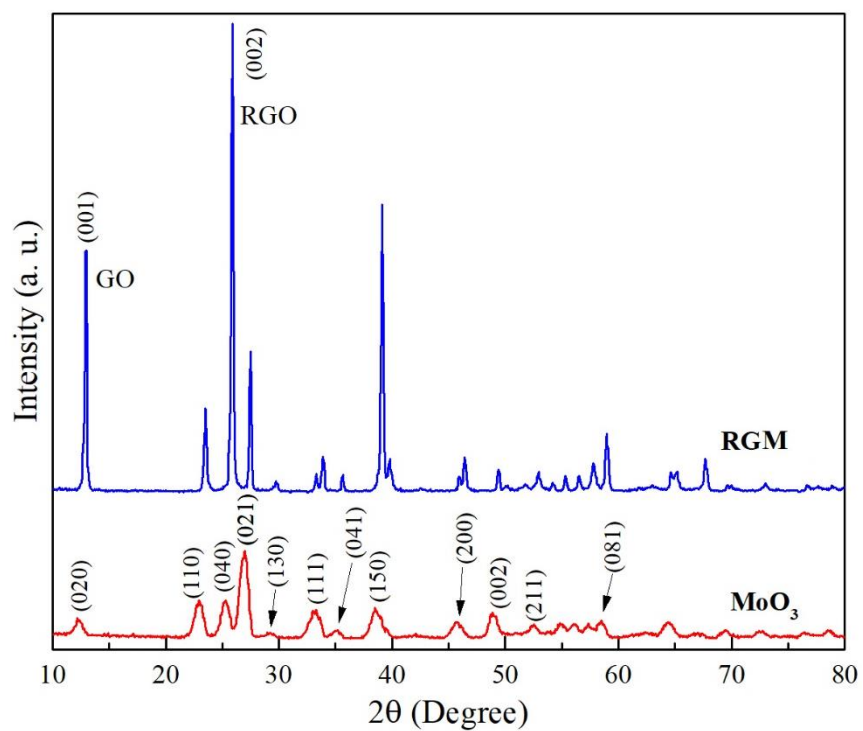


Figure 3: XRD patterns of MoO₃ and RGM, which indicates the crystallization of MoO₃ in the orthorhombic crystalline phase.

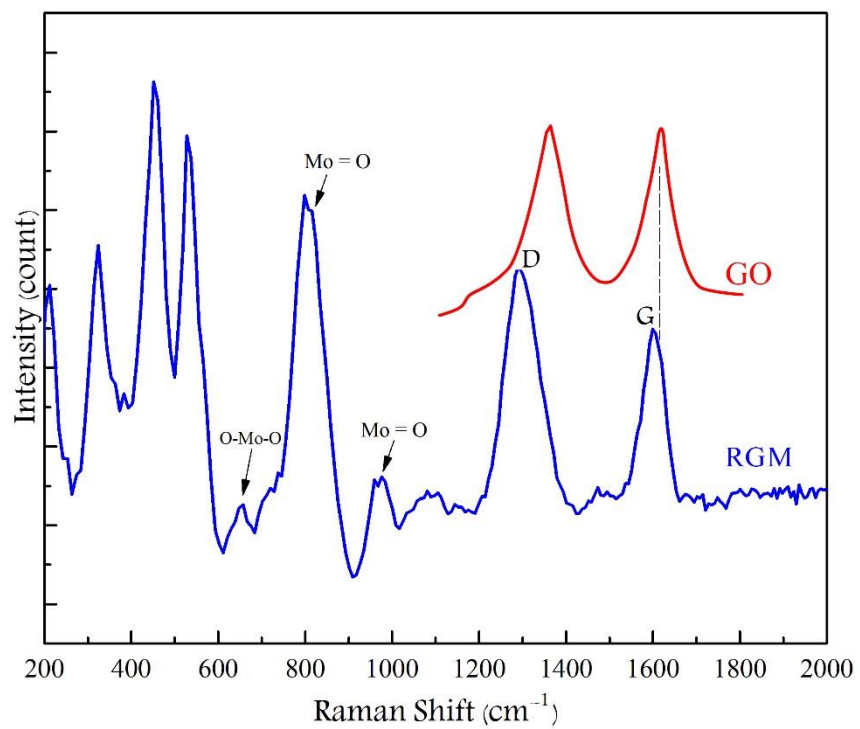


Figure 4: Raman shift of RGM compared with GO.

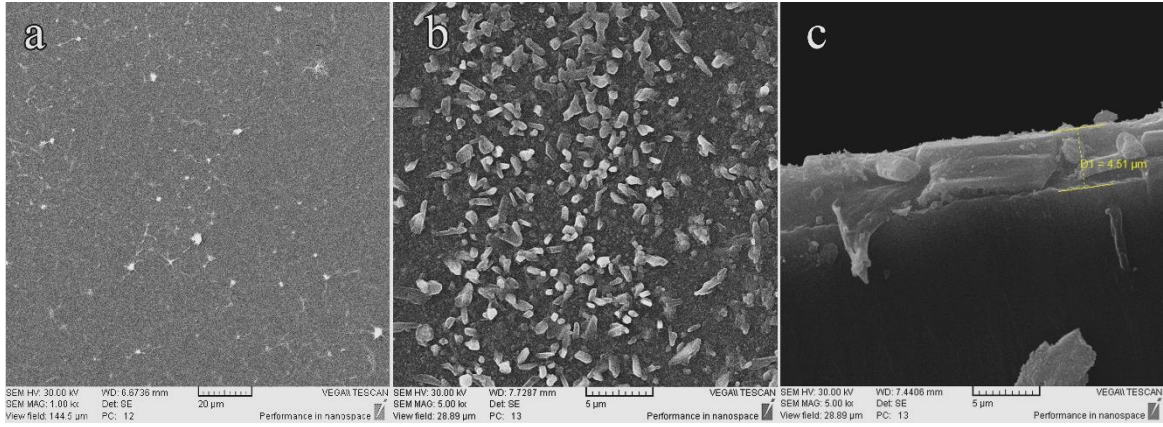


Figure 5: FESEM images of electrode surface deposited with RGM (a) before, (b) after annealing at 400 °C and (c) cross-section of the electrode.

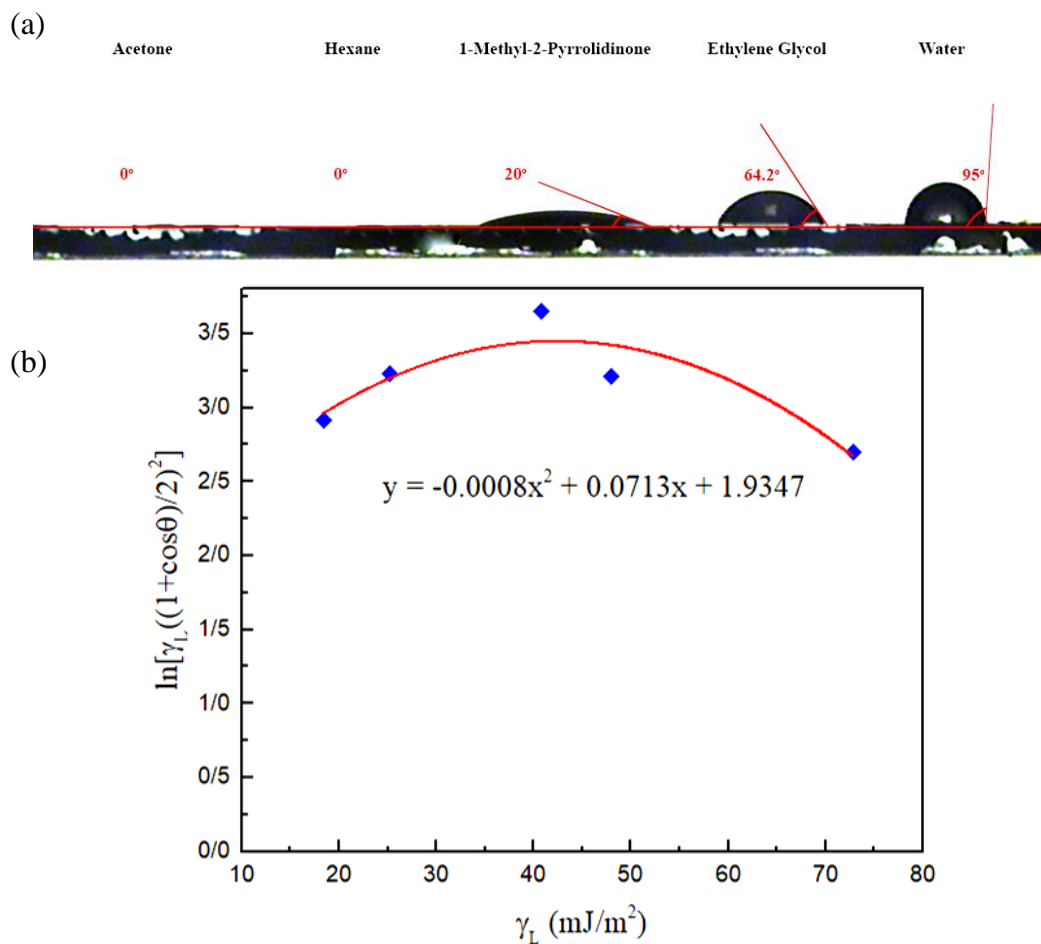


Figure 6: (a) Images of five various liquid droplets on the RGM surface and (b) the contact angle of each of them. Neumann's equation of state curve.

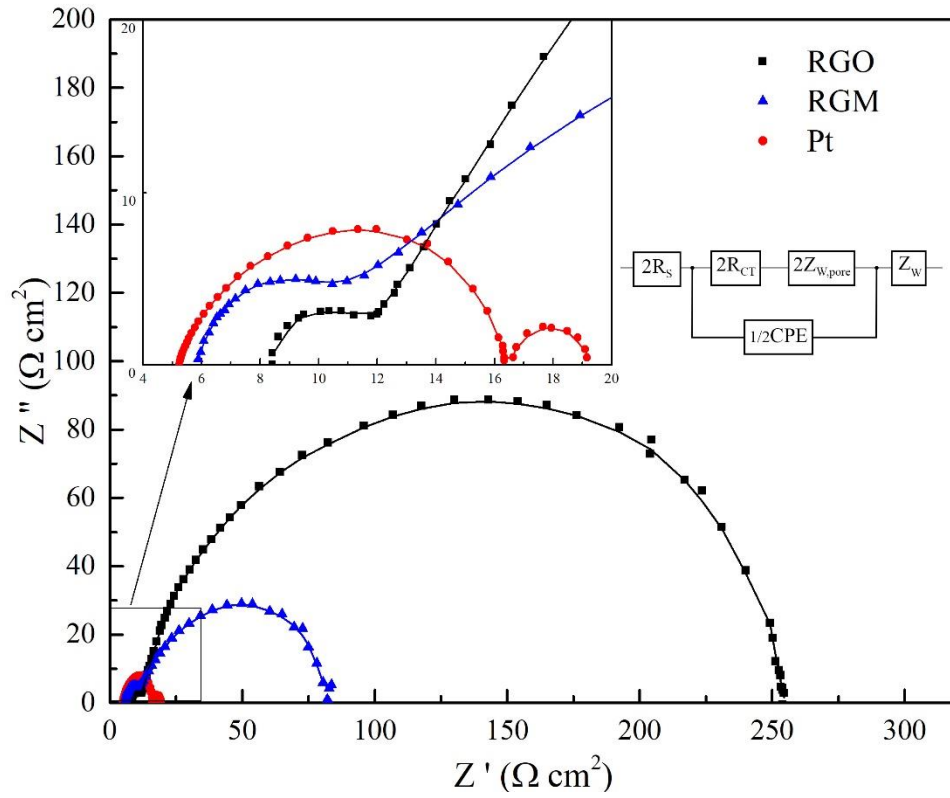


Figure 7: The Nyquist plots of symmetrical dummy cells fabricated with RGO, RGM and Pt. Left inset: magnified curves in the high-frequency region. Right inset: Equivalent circuit diagram for fitting the impedance spectra of a dummy cell.

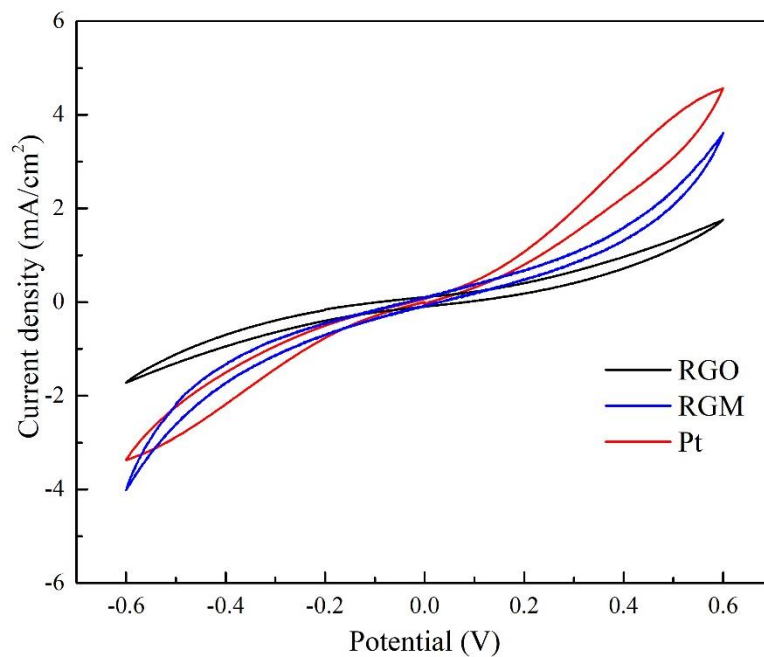


Figure 8: Cyclic Voltammogram plot of symmetrical dummy cells for RGO, RGM and Pt.

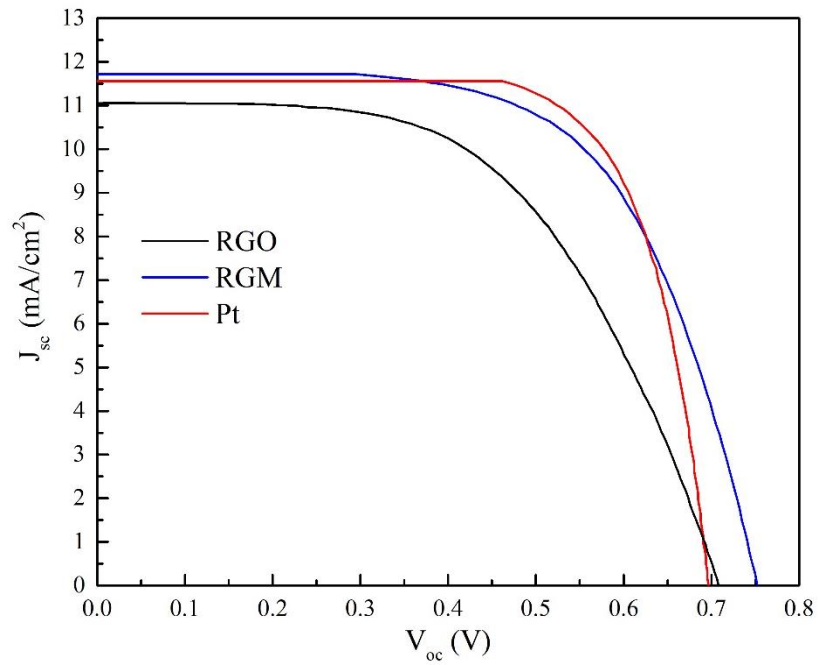


Figure 9: J-V plot of Photoelectrochemical cell of RGO, RGM, and Pt as a counter electrodes with the identical photoanode.

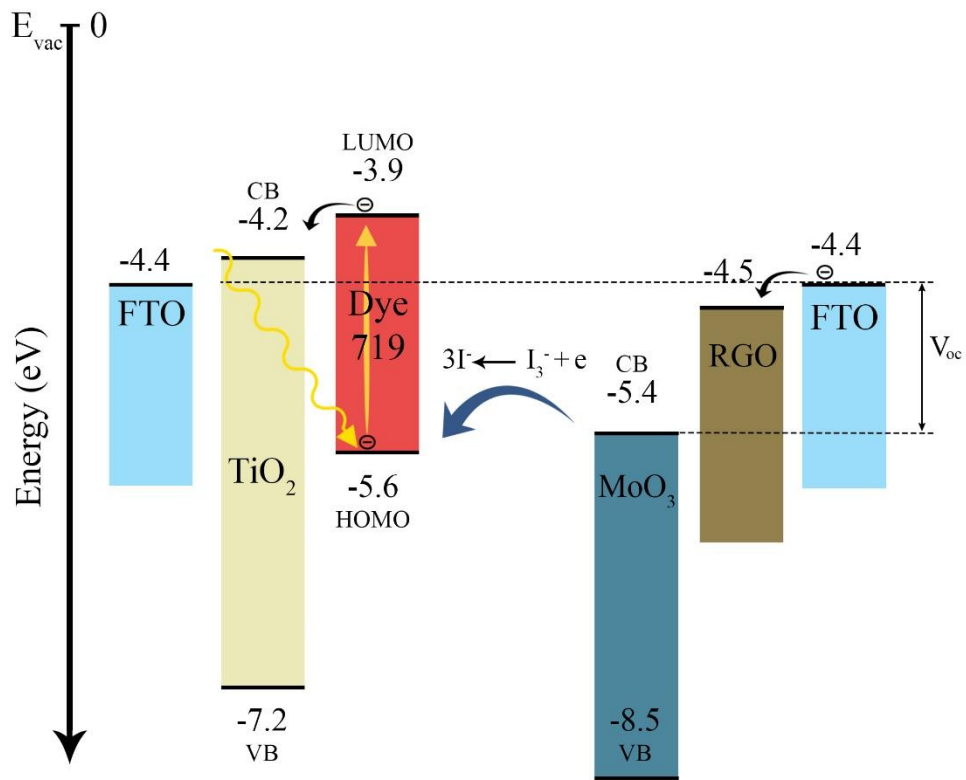


Figure 10: Schematic of energy levels in different layers of a photovoltaic cell [60]

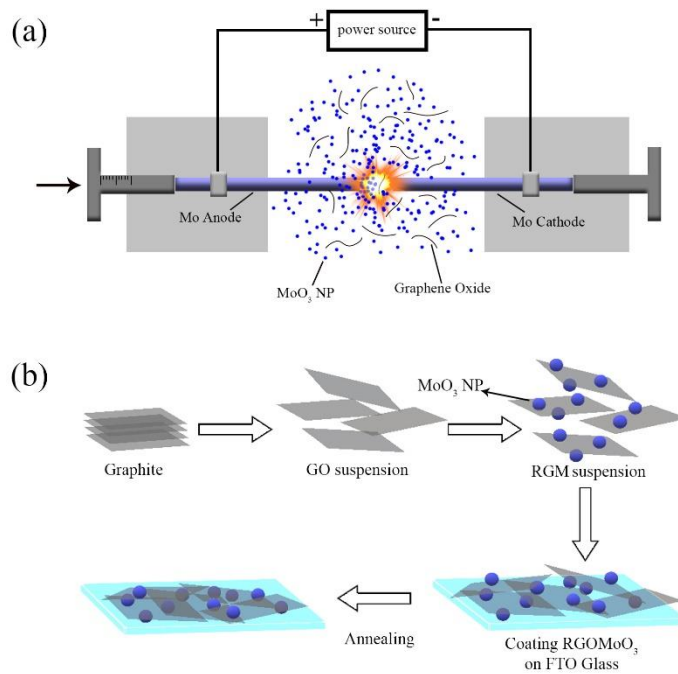


Figure 11: (a) Schematic of the arc discharge set-up, (b) Schematic illustration of the synthesis and coating process of the cathode.

References

1. Zhang, J., et al., *Electrochemically polymerized poly (3, 4-phenylenedioxythiophene) as efficient and transparent counter electrode for dye sensitized solar cells*. *Electrochimica Acta*, 2019. **300**: p. 482-488.
2. Browne, M.P., Z. Sofer, and M. Pumera, *Layered and two dimensional metal oxides for electrochemical energy conversion*. *Energy & Environmental Science*, 2019. **12**(1): p. 41-58.
3. Mackay, D.T., G.M. Norton, and S. Miller, *Lithium-ion batteries with nanostructured electrodes*. 2019, US Patent App. 14/762,691.
4. Calogero, G., et al., *Absorption spectra, thermal analysis, photoelectrochemical characterization and stability test of vegetable-based dye-sensitized solar cells*. *Optical Materials*, 2019. **88**: p. 24-29.
5. Shin, S.S., et al., *Energy-level engineering of the electron transporting layer for improving open-circuit voltage in dye and perovskite-based solar cells*. *Energy & Environmental Science*, 2019.
6. Pandey, A., et al., *Natural Sensitizers and Their Applications in Dye-Sensitized Solar Cell*, in *Environmental Biotechnology: For Sustainable Future*. 2019, Springer. p. 375-401.
7. Nguyen, P.T., et al., *Application of deep eutectic solvent from phenol and choline chloride in electrolyte to improve stability performance in dye-sensitized solar cells*. *Journal of Molecular Liquids*, 2019. **277**: p. 157-162.
8. Li, L., et al., *Electrospinning synthesis and electrocatalytic performance of iron oxide/carbon nanofibers composites as a low-cost efficient Pt-free counter electrode for dye-sensitized solar cells*. *Applied Surface Science*, 2019. **475**: p. 109-116.
9. Roy-Mayhew, J.D., et al., *Functionalized graphene as a catalytic counter electrode in dye-sensitized solar cells*. *ACS nano*, 2010. **4**(10): p. 6203-6211.
10. Jo, Y., et al., *Highly interconnected ordered mesoporous carbon-carbon nanotube nanocomposites: Pt-free, highly efficient, and durable counter electrodes for dye-sensitized solar cells*. *Chemical Communications*, 2012. **48**(65): p. 8057-8059.
11. Wu, M., et al., *Low-cost dye-sensitized solar cell based on nine kinds of carbon counter electrodes*. *Energy & Environmental Science*, 2011. **4**(6): p. 2308-2315.
12. O'regan, B. and M. Grätzel, *A low-cost, high-efficiency solar cell based on dye-sensitized colloidal TiO₂ films*. *nature*, 1991. **353**(6346): p. 737.
13. Jena, A., et al., *Dye sensitized solar cells: a review*. *Transactions of the Indian Ceramic Society*, 2012. **71**(1): p. 1-16.
14. Nan, H., et al., *Economically synthesized NiCo₂S₄/reduced graphene oxide composite as efficient counter electrode in dye-sensitized solar cell*. *Applied Surface Science*, 2018. **437**: p. 227-232.
15. Lickleder, M., et al., *Ordered Nanotubular Titanium Disulfide (TiS₂) Structures: Synthesis and Use as Counter Electrodes in Dye Sensitized Solar Cells (DSSCs)*. *Journal of The Electrochemical Society*, 2019. **166**(5): p. H3009-H3013.
16. Wang, L. and M. Pumera, *Electrochemical catalysis at low dimensional carbons: graphene, carbon nanotubes and beyond—a review*. *Applied Materials Today*, 2016. **5**: p. 134-141.

17. Navalon, S., et al., *Active sites on graphene-based materials as metal-free catalysts*. Chemical Society Reviews, 2017. **46**(15): p. 4501-4529.
18. Zhang, D., et al., *Graphene-based counter electrode for dye-sensitized solar cells*. Carbon, 2011. **49**(15): p. 5382-5388.
19. Shao, Y., et al., *Nitrogen-doped graphene and its electrochemical applications*. Journal of Materials Chemistry, 2010. **20**(35): p. 7491-7496.
20. Li, W., et al., *Sol-gel design strategy for ultradispersed TiO₂ nanoparticles on graphene for high-performance lithium ion batteries*. Journal of the American Chemical Society, 2013. **135**(49): p. 18300-18303.
21. Kavan, L., J.H. Yum, and M. Grätzel, *Optically transparent cathode for dye-sensitized solar cells based on graphene nanoplatelets*. ACS Nano, 2010. **5**(1): p. 165-172.
22. Choi, H., et al., *Graphene counter electrodes for dye-sensitized solar cells prepared by electrophoretic deposition*. Journal of Materials Chemistry, 2011. **21**(21): p. 7548-7551.
23. Jang, S.-Y., et al., *Electrodynamically sprayed thin films of aqueous dispersible graphene nanosheets: highly efficient cathodes for dye-sensitized solar cells*. ACS applied materials & interfaces, 2012. **4**(7): p. 3500-3507.
24. Chen, M. and L.-L. Shao, *Review on the recent progress of carbon counter electrodes for dye-sensitized solar cells*. Chemical Engineering Journal, 2016. **304**: p. 629-645.
25. Wongkrua, P., T. Thongtem, and S. Thongtem, *Synthesis of h - and α -MoO₃ by refluxing and calcination combination: phase and morphology transformation, photocatalysis, and photosensitization*. Journal of Nanomaterials, 2013. **2013**: p. 79.
26. Nadimicherla, R., et al., *Electrochemical performance of new α -MoO₃ nanobelt cathode materials for rechargeable Li-ion batteries*. Solid State Sciences, 2014. **34**: p. 43-48.
27. Datta, R., et al., *Highly active two dimensional α -MoO_{3-x} for the electrocatalytic hydrogen evolution reaction*. Journal of Materials Chemistry A, 2017. **5**(46): p. 24223-24231.
28. Chernova, N.A., et al., *Layered vanadium and molybdenum oxides: batteries and electrochromics*. Journal of Materials Chemistry, 2009. **19**(17): p. 2526-2552.
29. Mai, L.Q., et al., *Lithiated MoO₃ nanobelts with greatly improved performance for lithium batteries*. Advanced Materials, 2007. **19**(21): p. 3712-3716.
30. Luo, Z., et al., *Mesoporous MoO_{3-x} material as an efficient electrocatalyst for hydrogen evolution reactions*. Advanced Energy Materials, 2016. **6**(16): p. 1600528.
31. Li, L., et al., *P Doped MoO_{3-x} Nanosheets as Efficient and Stable Electrocatalysts for Hydrogen Evolution*. Small, 2017. **13**(25): p. 1700441.
32. Zhao, Y., L. Wang, and H.R. Byon, *High-performance rechargeable lithium-iodine batteries using triiodide/iodide redox couples in an aqueous cathode*. Nature communications, 2013. **4**: p. 1896.
33. Bao, Q., et al., *Electronic structures of MoO₃-based charge generation layer for tandem organic light-emitting diodes*. Applied physics letters, 2010. **97**(6): p. 172.
34. White, R.T., E.S. Thibau, and Z.-H. Lu, *Interface structure of MoO₃ on organic semiconductors*. Scientific reports, 2016. **6**: p. 21109.
35. Meyer, J., et al., *Metal oxide induced charge transfer doping and band alignment of graphene electrodes for efficient organic light emitting diodes*. Scientific reports, 2014. **4**: p. 5380.

36. Zheng, Q., et al., *Solution-Processed Composite Interfacial Layer of MoO_x-Doped Graphene Oxide for Robust Hole Injection in Organic Light-Emitting Diode*. *physica status solidi (RRL)–Rapid Research Letters*, 2018. **12**(4): p. 1700434.
37. Hummers Jr, W.S. and R.E. Offeman, *Preparation of graphitic oxide*. *Journal of the american chemical society*, 1958. **80**(6): p. 1339-1339.
38. Hosseini, F., R. Rasuli, and V. Jafarian, *Immobilized WO₃ nanoparticles on graphene oxide as a photo-induced antibacterial agent against UV-resistant Bacillus pumilus*. *Journal of Physics D: Applied Physics*, 2018. **51**(14): p. 145403.
39. Adineh, E. and R. Rasuli, *Facile synthesis of decorated graphene oxide sheets with WO₃ nanoparticles*. *Applied Physics A*, 2015. **120**(4): p. 1587-1592.
40. Ren, P.-G., et al., *Temperature dependence of graphene oxide reduced by hydrazine hydrate*. *Nanotechnology*, 2010. **22**(5): p. 055705.
41. Kumar, N., et al., *Effect of graphene oxide doping on superconducting properties of bulk MgB₂*. *Superconductor Science and Technology*, 2013. **26**(9): p. 095008.
42. Zhang, C., et al., *Facile synthesis and strongly microstructure-dependent electrochemical properties of graphene/manganese dioxide composites for supercapacitors*. *Nanoscale research letters*, 2014. **9**(1): p. 490.
43. Paulchamy, B., G. Arthi, and B. Lignesh, *A simple approach to stepwise synthesis of graphene oxide nanomaterial*. *Journal of Nanomedicine & Nanotechnology*, 2015. **6**(1): p. 1.
44. McAllister, M.J., et al., *Single sheet functionalized graphene by oxidation and thermal expansion of graphite*. *Chemistry of materials*, 2007. **19**(18): p. 4396-4404.
45. Ferrari, A.C., et al., *Raman spectrum of graphene and graphene layers*. *Physical review letters*, 2006. **97**(18): p. 187401.
46. Dong, Y., et al., *Wrinkled-graphene enriched MoO₃ nanobelts with increased conductivity and reduced stress for enhanced electrochemical performance*. *Physical Chemistry Chemical Physics*, 2013. **15**(40): p. 17165-17170.
47. King, A.A., et al., *A New Raman Metric for the Characterisation of Graphene oxide and its Derivatives*. *Scientific reports*, 2016. **6**: p. 19491.
48. Subrahmanyam, K., et al., *A study of graphenes prepared by different methods: characterization, properties and solubilization*. *Journal of Materials Chemistry*, 2008. **18**(13): p. 1517-1523.
49. Noerochim, L., et al., *Rapid synthesis of free-standing MoO₃/Graphene films by the microwave hydrothermal method as cathode for bendable lithium batteries*. *Journal of Power Sources*, 2013. **228**: p. 198-205.
50. Bai, S., et al., *Synthesis of MoO₃/reduced graphene oxide hybrids and mechanism of enhancing H₂S sensing performances*. *Sensors and Actuators B: Chemical*, 2015. **216**: p. 113-120.
51. Li, D. and A. Neumann, *Equation of state for interfacial tensions of solid-liquid systems*. *Advances in Colloid and Interface Science*, 1992. **39**: p. 299-345.
52. Kavan, L., et al., *Graphene Nanoplatelet Cathode for Co(III)/(II) Mediated Dye-Sensitized Solar Cells*. *ACS Nano*, 2011. **5**(11): p. 9171-9178.

53. Kavan, L., J.-H. Yum, and M. Grätzel, *Graphene Nanoplatelets Outperforming Platinum as the Electrocatalyst in Co-Bipyridine-Mediated Dye-Sensitized Solar Cells*. Nano Letters, 2011. **11**(12): p. 5501-5506.
54. Sahito, I.A., et al., *Graphene nanosheets as counter electrode with phenoxazine dye for efficient dye sensitized solar cell*. Organic Electronics, 2017. **44**: p. 32-41.
55. Wang, G., et al., *Low-cost counter electrodes based on nitrogen-doped porous carbon nanorods for dye-sensitized solar cells*. Materials Science in Semiconductor Processing, 2017. **63**: p. 190-195.
56. Ma, J., W. Shen, and F. Yu, *Graphene-enhanced three-dimensional structures of MoS₂ nanosheets as a counter electrode for Pt-free efficient dye-sensitized solar cells*. Journal of Power Sources, 2017. **351**: p. 58-66.
57. Chen, M., et al., *Mesoporous carbon counter electrode materials for dye-sensitized solar cells: the effect of structural mesopore ordering*. Chemical Engineering Journal, 2014. **256**: p. 23-31.
58. Veerappan, G., K. Bojan, and S.-W. Rhee, *Sub-micrometer-sized graphite as a conducting and catalytic counter electrode for dye-sensitized solar cells*. ACS applied materials & interfaces, 2011. **3**(3): p. 857-862.
59. Dong, J., et al., *Nickel selenide/reduced graphene oxide nanocomposite as counter electrode for high efficient dye-sensitized solar cells*. Journal of colloid and interface science, 2017. **498**: p. 217-222.
60. Wang, X., et al., *Tandem colloidal quantum dot solar cells employing a graded recombination layer*. Nature Photonics, 2011. **5**(8): p. 480.